HiSST: 2nd International Conference on
High-Speed Vehicle Science & Technology
16–19 May 2022, Bruges, Belgium

Investigation of Shock Patterns around a Double-Wedge for Hypersonic Flows in Thermochemical Non-Equilibrium

Maxime Lalande[1], *Chay W. C. Atkins*[2], *Ralf Deiterding*[3]

Abstract

Numerical simulations of hypersonic viscous flow in thermochemical non-equilibrium over a double wedge with high Mach and high enthalpy inflow conditions are performed to investigate shock pattern transition. First, simulations for varying second wedge angle are conducted in order to classify the shock patterns. Then, the effects of the thermochemistry on shock pattern transition are investigated by comparing simulations with air, nitrogen and an ideal gas flow. The highlighted effects of the second wedge angle, time and thermochemistry modelling on pattern transition are supported by a shock polar analysis. Finally, quantitative transition criteria are provided to summarise the influence of these three parameters.

Keywords: *Numerical simulation, Shock patterns, Shock-boundary layer interaction*

Nomenclature

Latin

BS – Bow Shock
CC – Compression Corner
CD – Contact Discontinuity
EC – Expansion Corner
EW – Expansion Waves
L_1 – First Wedge Length
L_2 – Second Wedge Length
LS – Leading Edge Shock
RS – Reattachment Shock
RS_i – Induced Reattachment Shock
SS – Separation Shock
TP – Triple Point
TS – Transmitted Shock
p – Pressure

Greek

γ – Adiabatic Gas Constant
θ – Total Deflection Angle
θ_1 – First Wedge Angle
θ_2 – Second Wedge Angle

1. Introduction

In addition to the naturally high aerothermal heating due to the high speed of hypersonic flows, shock-shock and shock-boundary layer interactions lead to the generation of various shock patterns that can be responsible for intense and localised heat flux peaks on the surface, which may fatally damage the structure. In that respect, it is paramount for hypersonic vehicles design to be able to predict the shock pattern that will occur in flight conditions in order to design an appropriate thermal protection system.

A first comprehensive study of the shock-shock interaction (SSI) is attributed to Edney [1], who experimentally investigated the impingement of an oblique shock wave generated by the sharp leading edge of a flat plate on a bow shock generated by a cylinder in FFA's Hyp 200 tunnel. Depending on the angle of

[1] *Visiting Post-Graduate Student, Aerodynamics and Flight Mechanics Research Group, University of Southampton, Boldrewood Campus, Southampton SO16 7QF, UK, m.lalande@soton.ac.uk*
[2] *PhD Student, Aerodynamics and Flight Mechanics Research Group, University of Southampton, Boldrewood Campus, Southampton SO16 7QF, UK, c.w.atkins@soton.ac.uk*
[3] *Professor, Aerodynamics and Flight Mechanics Research Group, University of Southampton, Boldrewood Campus, Southampton SO16 7QF, UK, r.deiterding@soton.ac.uk*

impact, he found six types of shock reflection patterns nowadays known as Edney patterns [2]. Among these patterns, some are more dramatic in local heat flux than others. For Types III, IV and V, there is a transmitted shock (Types III and VI) or a supersonic jet (Type IV) directly impinging the surface, which is responsible for high heat and pressure load in a localised area. The typical example of the risks generated by this mechanism is that of the American military hypersonic aircraft X-15A-2 which, during an experimental flight in 1967, saw part of its structure perforated due to shock reflections.

In addition to SSI, shock boundary layer interaction (SBLI) may occur. In particular, when an incident shock wave impinges a boundary layer, it creates an adverse pressure gradient which causes a separation bubble. A separation shock (SS) forms upstream of the bubble, and a reattachment shock (RS) downstream. These new shocks will potentially interact with one another or with other external shocks.

In this study, the shock interactions around a double wedge are investigated, see Fig. 1. An oblique and attached shock is generated at the sharp leading edge of the fore body, while the second wedge generates a detached bow shock. Moreover, the compression corner is responsible for a separation of the boundary layer at the end of the fore body, resulting in a separation and reattachment shocks. Numerous experimental and numerical studies have been carried out to classify the interaction patterns around double wedges in a manner similar to Edney's.

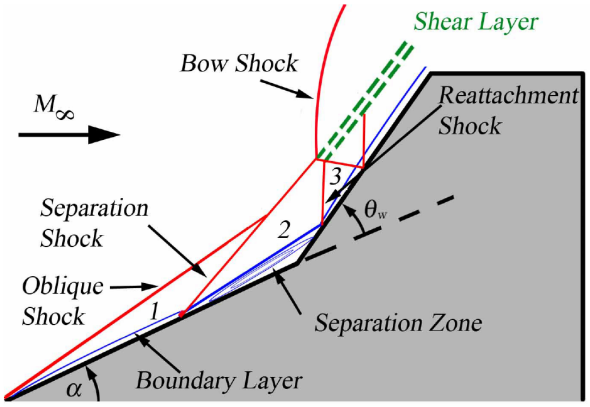

Fig 1. Simplified diagram of SSI and SBLI around a double wedge [3]

Olejniczak et al. numerically investigated the interaction of shocks on a double wedge for an inviscid flow with a perfect gas assumption [4]. Under these conditions, the thermochemistry of the gas as well as the viscosity are not taken into account, so there is no boundary layer or shock induced by a separation bubble. The authors found Edney shock patterns of Type IV, V and VI, as well as a new pattern called VIr, specific to the double wedge geometry. The transition from a Type VI to a Type V pattern occurs progressively as the second wedge angle θ_2 increases, whereas the transition from Type V to Type IV occurs abruptly beyond a critical angle. Li et al. repeated this study on the same double wedge configuration, taking into account the real gas effects to show that their influence is not negligible, still without considering the viscosity [5].

The experimental study from Swantek et al. [3] at the Hypervelocity Expansion Tube (HET) of the University of Illinois [6] has become a reference for many numerical studies. They performed Schlieren imaging and wall heat flux measurements for several test conditions of different Mach number and enthalpy values, for air or N_2, see Table 1. In particular, they showed that at low enthalpy, there was little difference between N_2 and air, as there were few thermochemical effects. On the other hand, at high enthalpy many chemical reactions occur, and there are noticeable differences regarding the flowfield establishment [7].

Pezzella et al. carried out a numerical study on the M7_8-N_2 and M7_8-air cases (Mach 7.14, stagnation enthalpy 8 MJ/kg, for N_2 and air) of Table 1 [8]. Thermochemical effects were modelled, and they

Table 1. Test conditions of Swantek et al. [3] with N_2 or air (76.3:23.3)

Freestream Parameters	**M5_4**	**M7_2**	**M7_8**	**M4_3.6**
Mach Number	5.12	7.11	7.14	4.01
Static Temperature, K	676	191	710	853
Static Pressure, kPa	8.13	0.391	0.78	18.3
Velocity, m/s	2664	1972	3812	2340
Density, kg/m^3	0.042	0.0071	0.0038	0.0747
Unit Reynolds Number, $10^6/m$	3.42	1.10	0.435	4.64
Stagnation Enthalpy, MJ/kg	4.1	2.1	8.0	3.6

showed the necessity to consider the transition of the boundary layer. Durna et al. studied the M7_2-N_2 case taking into account viscosity, thermophysical effects (*i.e.* variation of γ) but not the chemical dissociation reactions [9]. The results are not very consistent with the experimental schlieren images, but consistent with the measured wall heat flux. Simulations by Badr et al. for a 2D flow with a perfect gas assumption showed good agreements with the experiment regarding the wall heat flux for the low enthalpy M7_2 freestream conditions, but poorer agreement for the high enthalpy M7_8 case [10]. Better agreements were found by Komives et al. when simulating the M7_8 case assuming real gas effect for a 2D viscous flow [11]. The study of Hao et al. of the M7_8-N_2 case with unsteady, viscous, real gas effects and in 3D on infinite span simulations showed that the 3D simulations provided shock shapes more consistent with the experimental schlieren visualisation, as 2D simulations tend to over-predict the bow shock curvature [12]. The work of Reinert et al. on M7_8-N_2 and M7_8-air cases with unsteady, viscous, real gas effects and 3D on finite span simulations confirmed these results by showing excellent agreements for shock shape and good consistency for wall heat flux [13]. Therefore, the consideration of the viscosity and the real gas effects are essential to investigate high enthalpy flow around a double-wedge.

The focus of this work is on investigating the shock pattern transition around a double-wedge for hypersonic flows. This is done using a recently developed version of our in-house code AMROC (Adaptive Mesh Refinement in Object-oriented C++), which enables the coupling of a Cartesian Structured Adaptive Mesh Refinement (SAMR) solver for the off-body region with a so-called *strand*-mesh coupling for the near body region, so as to simulate 2D hypersonic viscous flows in thermochemical non-equilibrium with species-dependent viscosity [14, 15].

2. Classification of the Shock Patterns

2.1. Setting up of the simulations

The double wedge geometry is adopted from the experiment by Swantek et al. [3], with a fore body of angle $\theta_1 = 30°$ and length $L_1 = 50.8$ mm, and an aft body of length $L_2 = L_1/2 = 25.4$ mm. In their experiment, the second wedge angle was set to $\theta_2 = 55°$. However, in this work simulations have been carried out in the range of $\theta_2 = 45 - 60°$. The inflow condition considered is the high-Mach high-enthalpy M7_8 case of Swantek et al. [3], *i.e* a Mach number of 7.14 and a stagnation enthalpy of 8.0 MJ/kg.

The computational domain is a rectangle of size 0.09mm $\times$ 0.11mm, within which the solid structure of the double wedge is included. The AMROC code uses a Cartesian SAMR mesh for the off-body region and a structured mapped mesh for the near body region to solve the 2D Navier-Stokes equations with a no-slip wall boundary conditions. Starting from an irregular discretisation of the surface, a strand mesh is generated in a direction normal to the wall. Figure 2 shows an example of mesh generation around a double wedge with this method. The Cartesian (blue) mesh is undergoing several automatic adaptation levels in order to capture the shocks, and the near body (red) mesh is grown from a given triangulation of the surface using an hyperbolic tangent stretching function. Overset coupling routines are used to enable connecting the solution computed in the two regions. The thermochemical modelling

is performed thanks to the coupling with the open source code Mutation++ [16]. The external flow is initialised with the test condition of the M7_8 case. A time-explicit scheme with a target CFL number of 0.85 is used for the time integration of the Cartesian off-body mesh, whereas an implicit scheme with a target CFL number of 25 is used for the time integration of the near-body mesh. The simulation is run for $t = 240\mu s$.

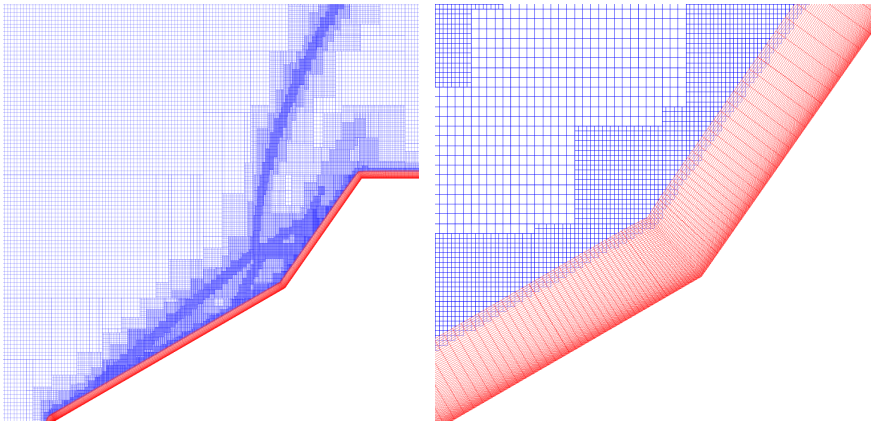

Fig 2. Cartesian SAMR (blue) and near-body (red) mesh generation around a double wedge. Global view of the mesh (left) and zoom into compression corner (right)

The mesh design has been validated through a convergence study by comparing the simulations for three increasingly finer meshes. For the first one, referred as the Base Mesh (BM), the Cartesian mesh is a regular grid of 150×150 elements, with 4 possible levels of adaptive mesh refinement to capture the strong gradients. The near-body mesh is made of $(250 + 90 + 40) \times 70$ elements, *i.e.* 250 elements along the fore body ($L_1 = 50.8$ mm), 90 elements along the aft body ($L_1 = 25.4$ mm), 40 elements along the back of the second wedge and 70 elements in the normal direction (thickness of 1.5 mm). The two finer meshes FM1 and FM2 are also reported in Table 2.

Table 2. Investigated meshes for the grid convergence study

Mesh Name	Cartesian Mesh	Near-Body Mesh
Base Mesh (BM)	150*150 on 4 levels	(250+90+40)*70
Fine Mesh 1 (FM1)	170*170 on 4 levels	(250+120+50)*70
Fine Mesh 2 (FM2)	200*200 on 4 levels	(250+150+50)*90

The simulations for the three meshes are compared for $\theta_2 = 55°$ for a nitrogen flow. The wall heat flux computed at $t = [60, 85, 120, 180, 240]\mu s$ are plotted in Fig. 3. The graph shows excellent agreements between the different meshes, and confirms the base mesh validity.

The global consistency is assessed by comparing the density gradient field at different numerical times. Figure 4 compares the density gradient at $t = 85\mu s$ obtained with the three meshes, which exhibit good agreement. Hence, the Base Mesh has been used for this study.

First, a parametric study of the influence of the second wedge angle $\theta_2 = 45 - 60°$ is performed so as to explore the variety of possible shock patterns in this range of θ_2. The patterns computed are classified in the following. The fluid model is a nitrogen flow (two species N_2 and N with dissociation).

This classification is supported by a shock polar analysis, using our in-house shock polar code based on the Euler equations with Rankine-Hugoniot jump conditions [17], and coupled with the thermochemistry library Chemkin [18] to consider multi-species flow of temperature-dependant γ.

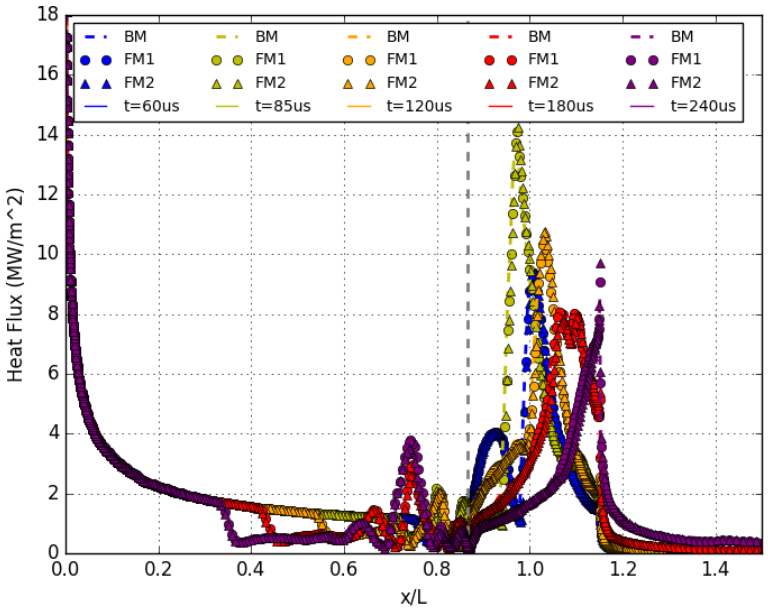

Fig 3. Wall heat flux computed at different numerical times for three meshes: Base Mesh (BM, dashed lines), Fine Mesh 1 (FM1, dotted markers) and Fine Mesh 2 (FM2, delta markers) - Dashed grey line represents the compression corner location

2.2. Type VI

A first shock structure that can be obtained is the so-called Type VI pattern. Like Edney's study, this pattern results from the regular reflection between the leading edge shock (LS) and the reattachment shock (RS) generated by the first and second wedge. From the triple point (TP) emanates a cone of expansion waves (EW) and a contact discontinuity (CD), or slip line. Figure 5a shows the gradient density computed by AMROC for a second wedge angle of $\theta_2 = 45°$ at computation time $t = 100\mu s$. The EW outgoing from the TP are nearly visible for this case. The solid red lines are the sonic lines (*i.e.* Mach=1). Figure 5b is the schematic diagram of the Type VI pattern. Region (0) is the inflow, (1) is the flow behind the LS, region (2) is behind the SS and (4) is behind the RS. The region (3) is the supersonic flow behind the TP, *i.e.* between the EW and the CD. The flow above the CD is indeed subsonic whereas it is supersonic below, as it can be seen thanks to the sonic line on Fig. 5a.

Figure 6 is the associated shock polar diagram. Points (0)-(4) on the shock polar plot correspond to the states (0)-(4) of the flow. On a shock polar diagram, it is plotted according to the total deflection angle of the flow θ and the pressure ratio p/p_0.

Naturally, state (0) has a zero deflection and a pressure ratio $p/p_0 = p_0/p_0 = 1$, since it's the inflow. The I-polar represents all the possible states $(p/p_0, \theta)$ behind a shock in (0). Since the flow in (1) has to be deflected by an angle $\theta_1 = 30°$ (first wedge angle) due to the non-slip condition, state (1) is on the I-polar at a total deflection angle $\theta = \theta_1 = 30°$. There are two possible solutions at $\theta = \theta_1$ on the I-polar, standing for the weak and strong shock solutions, however in nature the weak shock solution prevails. The R1-polar represents all the possible states behind a shock in (1). Region (2) is behind the SS, which is triggered by the separation bubble. One needs to know where to put state (2) on the R1-polar. From the AMROC simulation, one can get the total deflection angle in (2), and then set state (2) on the R1-polar. Note that this value is directly related to the SS, and so to the development of the separation bubble. In this way, one can apply the inviscid shock polar analysis to viscous simulation results.

State (4) is behind the states (2) and (1), and is supposed to have a total deflection equal to the second wedge angle $\theta_2 = 45°$ because of the non-slip condition. On the shock polar, (4) can both be defined as the point on R1-polar at $\theta = \theta_2$ or on the R2-polar at $\theta = \theta_2$. In this case, these two points are nearly the

(a) Base Mesh **(b)** Fine Mesh 1 **(c)** Fine Mesh 2

Fig 4. Density gradient comparison at $t = 85\mu s$ for increasingly finer meshes

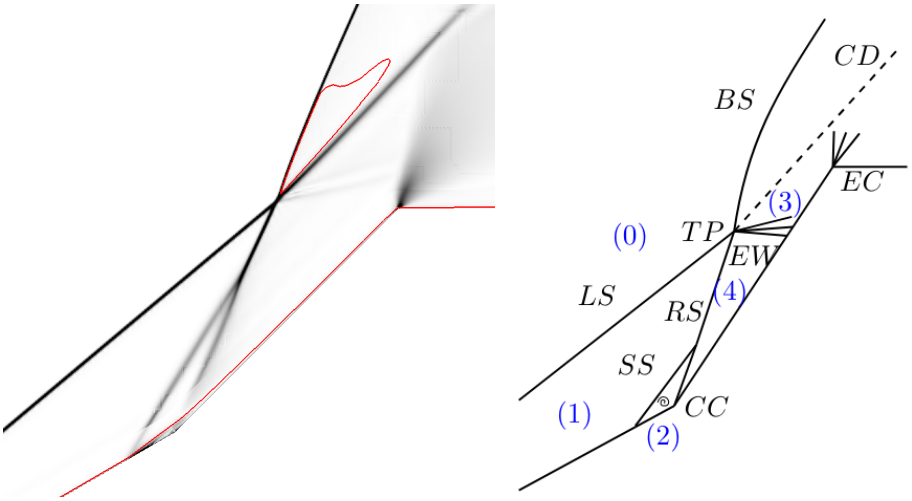

(a) AMROC simulation of case M7_8-N_2, $\theta_2 = 45°, t = 100\mu s$ **(b)** Schematic diagram

Fig 5. Type VI shock pattern around a double wedge

same on the shock polar, and we made the choice for the whole study to define (4) from the R2-polar. Moreover, there is no slip line outgoing from the TP formed by the SS and the RS, meaning that state (4) is homogeneous behind (1) and (2), which perfectly relates with the fact that R1 and R2-polar are equal at $\theta = \theta_2$.

State (3) is built differently on the shock polar. On the one hand, (3) is behind the BS so it should be somewhere on the I-polar. On the other hand, there is a cone of EW between (4) and (3), which is represented thanks to an isentropic line on a $(\theta, p/p_0)$ diagram, see 4-EW the dotted blue line on Fig. 6. Hence, (3) is the intersection of the I-polar and 4-EW.

One can note that points (3) and (4) are very close on the shock polar, meaning that states (3) and (4) are nearly the same in terms of θ and pressure ratio. This can explain the very weak expansion waves separating (3) and (4) on Fig. 5a.

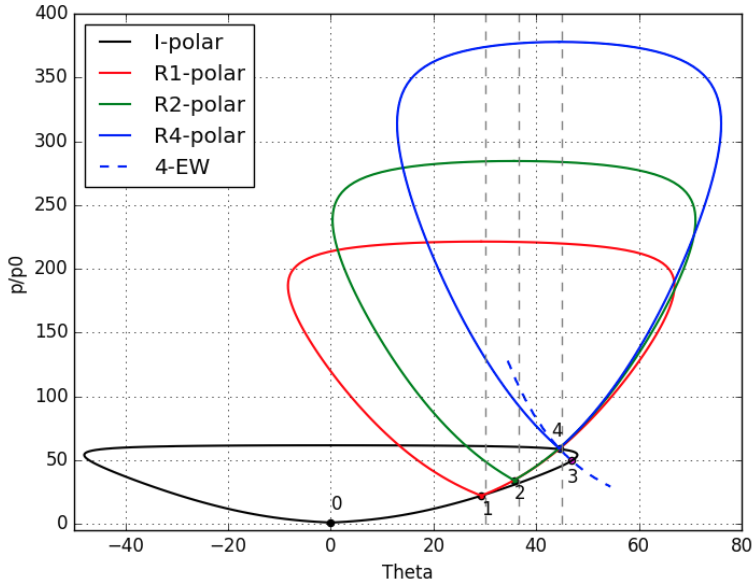

Fig 6. Shock polar for the M7_8-$N2$ case with $\theta_2 = 45°$

2.3. Type VI-TS

For greater second wedge angle, a transmitted shock (TS) emanates from the TP. This shock pattern is then denoted Type VI-TS. Figure 7a shows the density gradient computed at $t = 80\mu s$ for $\theta_2 = 47.5$, and Fig. 7b pictures a schematic diagram of this Type VI-TS pattern. There is still a regular reflection between LS and RS, with a single TP from which now emerges a CD and a TS impinging the aft body.

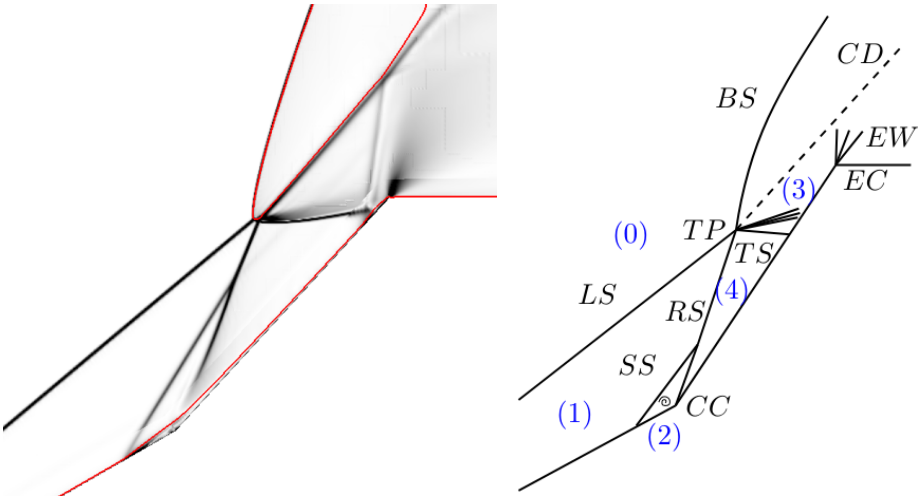

(a) AMROC simulation of case M7_8-N_2, $\theta_2 = 47.5°, t = 80\mu s$

(b) Schematic diagram

Fig 7. Type VI-TS shock pattern around a double wedge

Figure 8 shows the associated shock polar associated to the Type VI-TS pattern presented on Fig. 7. States (0)-(3) are similar to the previous case, since the inflow conditions are unchanged. However, as the second wedge angle θ_2 has been increased, and since state (4) must meet the deflection angle $\theta = \theta_2$, point (4) got displaced to the right on the R2-polar. As a consequence, the isentropic line outgoing from (4) does not intersect the I-polar anymore, explaining why there can not be a simple

expansion fan between (3) and (4). State (3) is still somewhere on the I-polar, but since we have no information on θ or p/p_0 behind the TS, it is impossible to build (3).

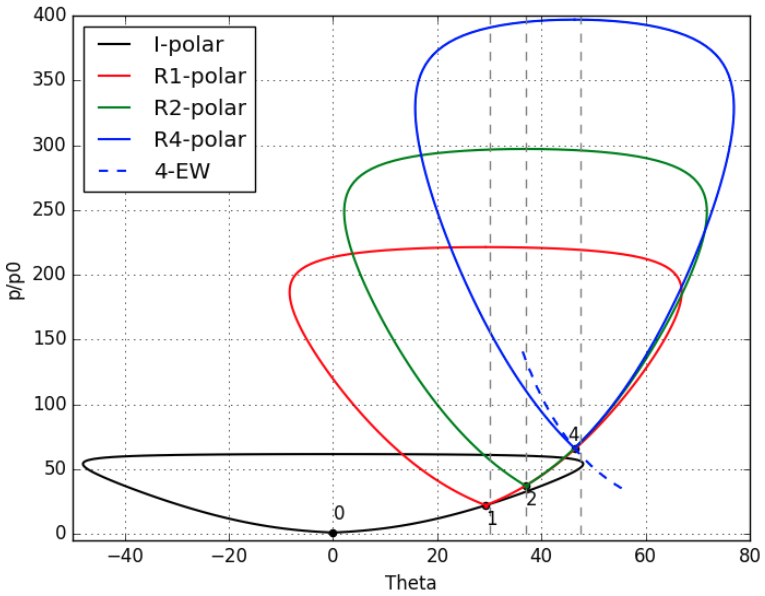

Fig 8. Shock polar for the M7_8-$N2$ case with $\theta_2 = 47.5°$

2.4. Type V-6S-2EW

Figure 9a shows the density gradient computed for $\theta_2 = 50°$ at $t = 70\mu s$, and Fig. 9b presents the associated schematic diagram. The connection of the RS and the LS into a single TP is not possible anymore, and the RS now impacts the TS in a regular reflection. The RS is slightly deflected behind its impingement with the TS, and is finally reflected into EW after meeting the CD. The TS directly impacts the aft body, leading to the formation of a small separation bubble in the boundary layer. This generates an induced reattachment shock (RS_i) which is reflected into EW on the CD. This shock structure is made of 6 shocks (LS, BS, SS, RS, TS, RS_i) and two expansion waves due to the reflection of the TS and RS_i on the CD. Hence, this pattern has been labelled Type V-6S-2EW.

Figure 10 is the shock polar associated to the simulation of Fig. 9. States (0)-(2) are built similarly to the previous case since the inflow conditions are unchanged. However, the RS is no longer impinging the TP made of the LS, BS and RS, so it is now possible to build (3) on the shock polar. State (3) is the intersection point between I and R1-polar on the left branch (or indirect branch) of R1-polar. As a matter of fact, the right (direct) and left (indirect) solutions are both theoretically possible, and the real solution has to be determined from the simulations.

State (5) corresponds to the region of the flow behind the TP formed by the regular reflection (RR) of the RS and the TS, below the EW. On the shock polar, point (5) is then defined as the intersection point between the R3 and R4-polars. Note that the R4 and R3-polars also both intersect the R1-polar in points (a) and (b). Theoretically, there is a common possible state (a) between (1) and (4) on the one hand, and (b) between (1) and (3) on the other, with (a) and (b) being distinct states. This would be the case of a Mach reflection, with a top TP made of (1)-(3)-(b) and a lower TP made of (1)-(4)-(a). However, since the total deflection angle of (a) is lower than that of (b), the two slip lines emerging from the two TP would be forming a diverging subsonic stream tube. Because the flow is returning to supersonic speed after a certain distance behind the Mach stem, it is impossible to have an accelerating subsonic flow in such a diverging stream tube. Hence, even though both MR and RR are theoretically possible at first sight, the only physically acceptable solution according to the shock polar is the RR for the RS and the TS. This is consistent with the Fig. 9a.

One can also build state (5'), see Fig. 9b. On the one hand, (5') is separated from (5) by an expansion

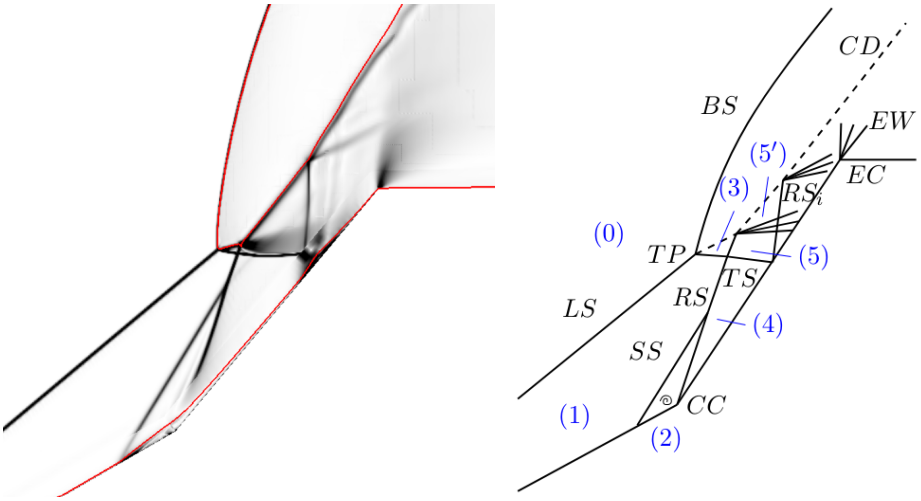

(a) AMROC simulation of case M7_8-N_2, $\theta_2 = 50°, t = 70\mu s$

(b) Schematic diagram

Fig 9. Type V-6S-2EW shock pattern around a double wedge

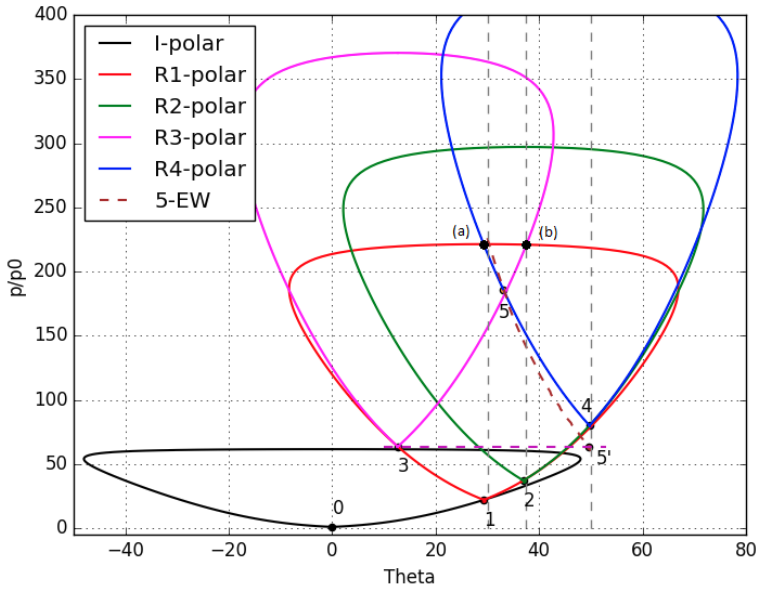

Fig 10. Shock polar for the M7_8-$N2$ case with $\theta_2 = 50°, t = 70\mu s$

fan, so state (5′) is somewhere on the isentropic line 5-EW outgoing from (5) on the $(\theta, p/p_0)$ diagram. On the other hand, (5′) is bounded by the CD, involving that the pressure ratio p/p_0 in (5′) is equal to p_3/p_0. This way it is possible to build (5′) as the intersection of 5-EW and the $p/p_0 = p_3/p_0$ lines.

2.5. Type V-6S-3EW

Figure 11a is the density gradient computed for inflow conditions and a geometry similar to the previous case, *i.e.* the M7_8-N_2 conditions with $\theta_2 = 50°$, but at a longer time $t = 150\mu s$. The shock structure obtained is different and depicted in Fig. 11b. The previous Type V-6S-2EW only stands as long as the SS merges with the RS. However, the separation bubble located just upstream from the compression corner (CC) grows over time, as a consequence the SS gets displaced upstream and its angle of incidence increases. The impingement point between the SS and the RS gets displaced upwards along the RS,

and finally separates so the SS impacts the TS. The SS is slightly deflected by the TS, and is reflected into EW on the CD. Since this shock pattern adds an EW, it is denoted Type V-6S-3EW.

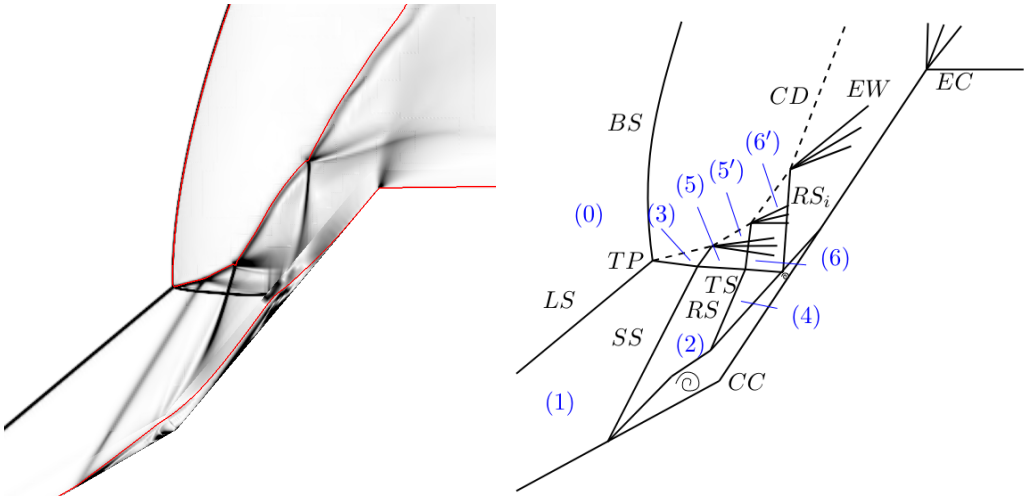

(a) AMROC simulation of case M7_8-N_2, $\theta_2 = 50°, t = 150\mu s$ **(b)** Schematic diagram

Fig 11. Type V-6S-3EW shock pattern around a double wedge

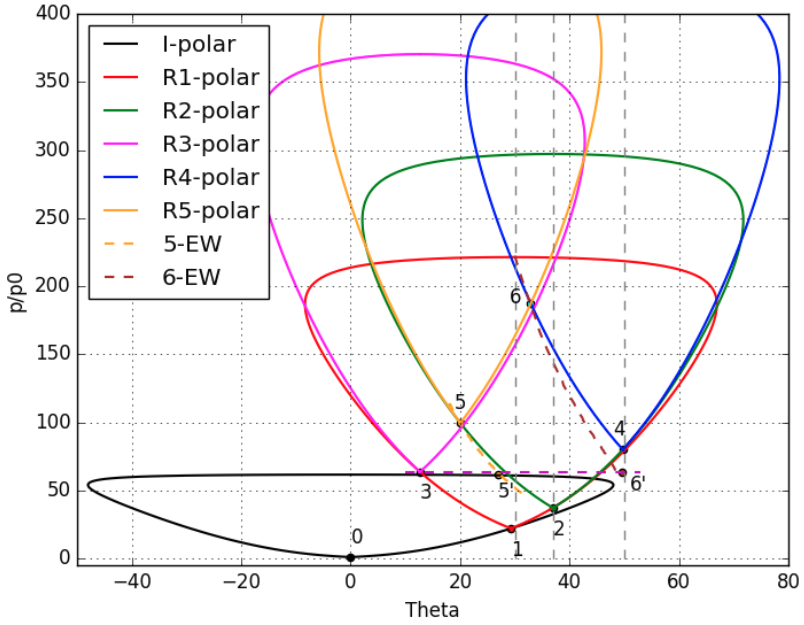

Fig 12. Shock polar for the M7_8-$N2$ case with $\theta_2 = 50°, t = 150\mu s$

Figure 12 shows the corresponding shock polars. Regions (0)-(2) are defined similarly to the previous cases. Region (3) is the intersection point between I and R1-polar on the left-branch of the R1-polar, for identical reasons as the Type V-6S-2EW. Region (4) is still defined as the weak shock solution on the R2-polar at $\theta = \theta_2 = 50°$, whereas for previous cases it could have also been defined on the R1-polar. Since (4) were behind both regions (1) and (2), for a Type V-6S-3EW structure, state (4) can only be built based on state (2). Region (5) is behind the RR of the SS and the TS, so state (5) is the intersection of the R2 and R3-polars. This point is inside the R1-polar, so the MR solution is physically impossible

and there must be a RR between the SS and the TS, which is consistent with the computations. Region (6) is downstream the RR between the RS and the TS. State (6) is then the intersection between R4 and R5-polar, and is inside the R2-polar which is consistent with a RR. States (5') and (6') are bounded by the CD and a cone of EW separating them respectively from (5) and (6). Hence, (5') and (6') are respectively the intersection of 5-EW and 6-EW with the $p/p_0 = p_3/p_0$ line.

2.6. Type V

The shock pattern corresponding to the Type V in the classification of Edney can be obtained for even greater second wedge angle. Figure 15a is the density gradient computed for $\theta_2 = 57.5°$ at $t = 30\mu s$, with the corresponding schematic diagram on Fig. 13b and shock polar on Fig. 14. The time is sufficiently small for the SS to still merge with the RS. The second wedge angle is now so large that the interaction between the RS and TS is no more a regular reflection (RR) but a Mach reflection (MR). There is a Mach stem (MS), which is a normal shock to the flow in (1), and behind which the flow is subsonic. This MS is bounded by two triple points. The upper TP is made of the ingoing TS and MS, and the outgoing RS. The lower TP is made of the ingoing MS and RS, and the outgoing TS. From each triple point also emanate a contact discontinuity. States (5) and (6) are behind the two TP, outside the region bounded by two CD.

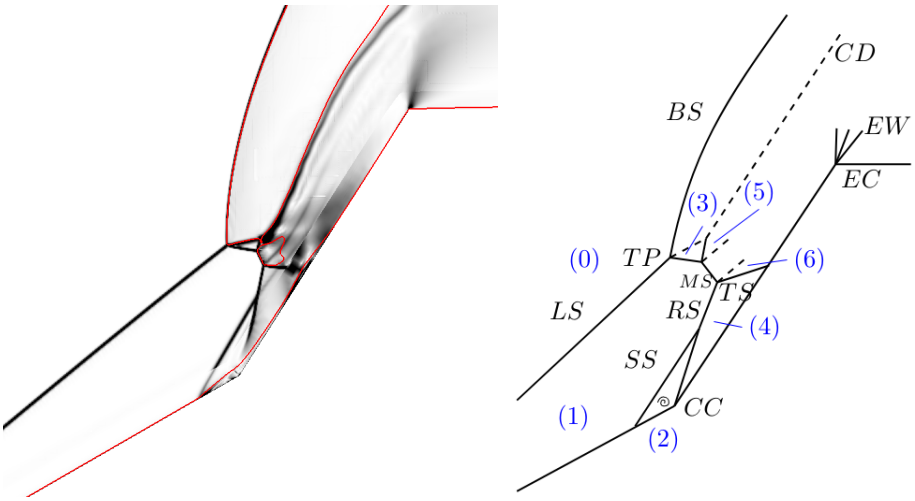

(a) AMROC simulation of case M7_8-N_2, $\theta_2 = 57.5°, t = 30\mu s$

(b) Schematic diagram

Fig 13. Type V shock pattern around a double wedge

States (0)-(4) are defined similarly to the Type V-6S-2EW. However in this case, the intersection between the R3 and R4-polar is no longer inside the R1-polar. Then, two theoretical solutions are possible. On the one hand, the intersection of R3 and R4 shows that there is a common possible state behind a shock standing in regions (3) and (4), *i.e.* there is a regular reflection of the TS and the RS, corresponding to a Type V-6S-2EW pattern. On the other hand, the R3 and R4-polars both intersect the R1-polar in points (5) and (6), corresponding to a possible Mach reflection with (5) the state behind the top TP, and (6) the one behind the lower TP. Since the total deflection angle of state (5) is lower than that of state (6), the subsonic stream tube bounded by the two slip lines is converging, which is physically admissible. From the shock polar, both the RR and the MR solutions are theoretically and physically possible. The real solution is the MR, according to the simulations with AMROC.

The Type V only subsists as long as the SS still merges with the RS. Figure 15 shows the computed density gradient at successive times. Initially, there is a Type V pattern for sufficiently low time $t = 30\mu s$. As the separation bubble grows and the SS onset location gets displaced upstream along the first wedge, the SS impacts the Mach stem at $t = 45\mu s$ and finally the TS at $t = 60\mu s$. So far, the Mach stem still stands, so this is still a Type V pattern. For longer time though, this Mach stem vanishes and the shock

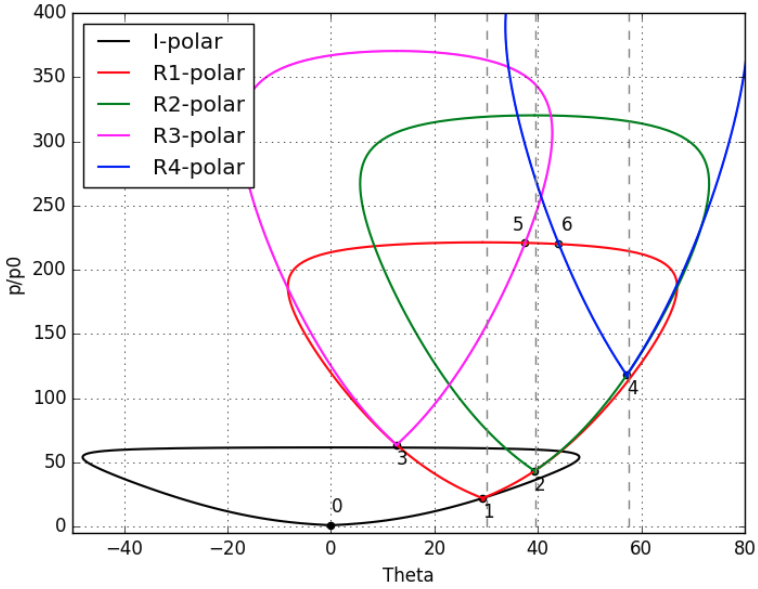

Fig 14. Shock polar for the M7_8-$N2$ case with $\theta_2 = 57.5°, t = 30\mu s$

pattern becomes a Type V-6S-3EW, see Fig. 15d.

3. Effect of the Thermochemistry on Shock Patterns Transition

Thermochemistry is a major feature of hypersonics, so it is reasonable to investigate its effect on the shock pattern transition. The density gradient and shock polar are compared for different fluid models: air, N_2 and an ideal gas. We recall that on the one hand, AMROC can model multi-species flow with non-constant specific heat capacity C_p and dissociation reactions, and on the other hand the shock polar code considers a non-reactive thermally perfect gas mixture, *i.e.* no dissociation and temperature-dependant heat ratio $\gamma = C_p/C_v$. The ideal gas is supposed to have the lowest thermochemical effects since it is considered as single diatomic gas (*i.e.* no dissociation) with constant C_p (*i.e.* calorically perfect) and $\gamma = 1.4$. Nitrogen flow brings up the two species N and N_2, with associated dissociation and recombination reactions and non-constant specific heat capacity C_p. The air flow is composed of the 5 species N_2, N, O_2, O, NO with associated chemical reactions and variable C_p, increasing the complexity of the thermochemical model compared to nitrogen flow. To sum up, thermochemical effects on shock pattern transition are investigated by comparing density gradients computed thanks to AMROC and the associated shock polar for air, nitrogen and an ideal gas, with simplest thermochemistry modelling for the ideal gas and most complex for the air flow.

Numerous cases have been computed for various θ_2 with air, N_2 and an ideal gas during the study, however only two cases are reported here. The first example is for a second wedge angle $\theta_2 = 45°$, at $t = 120\mu s$. Figure 16 compares the density gradient for the three fluid models, and Fig. 17 shows the associated shock polar. For the air flow, the shock pattern is a Type VI as there is a single triple point and no transmitted shock visible on Fig. 16a, and the isentropic line 4-EW outgoing from state (4) intersects the I-polar on the shock polar, see Fig. 17a. The shock pattern is similar for nitrogen, with nearly identical shock polar diagram. However for the ideal gas, the shock pattern looks like a Type VI-TS, which is a limiting case of the Type V-6S-2EW, as previously mentioned. This is confirmed by the shock polar, see Fig. 17c, since the isentropic line 4-EW does not intersect the I-polar. The polars for the ideal gas have a lower amplitude along both the θ_2 and p/p_0-axis compared to polars for air and N_2. Physically, the maximum admissible total deflection angle behind a given shock is greater if one considers a real gas instead of an ideal gas. In addition, the possible compression behind a given shock is higher for a real gas. This significantly limits the range of possible states behind shocks for an ideal gas, which could explain why for $\theta_2 = 45°$ the shock pattern is Type VI for both air and N_2 whereas it

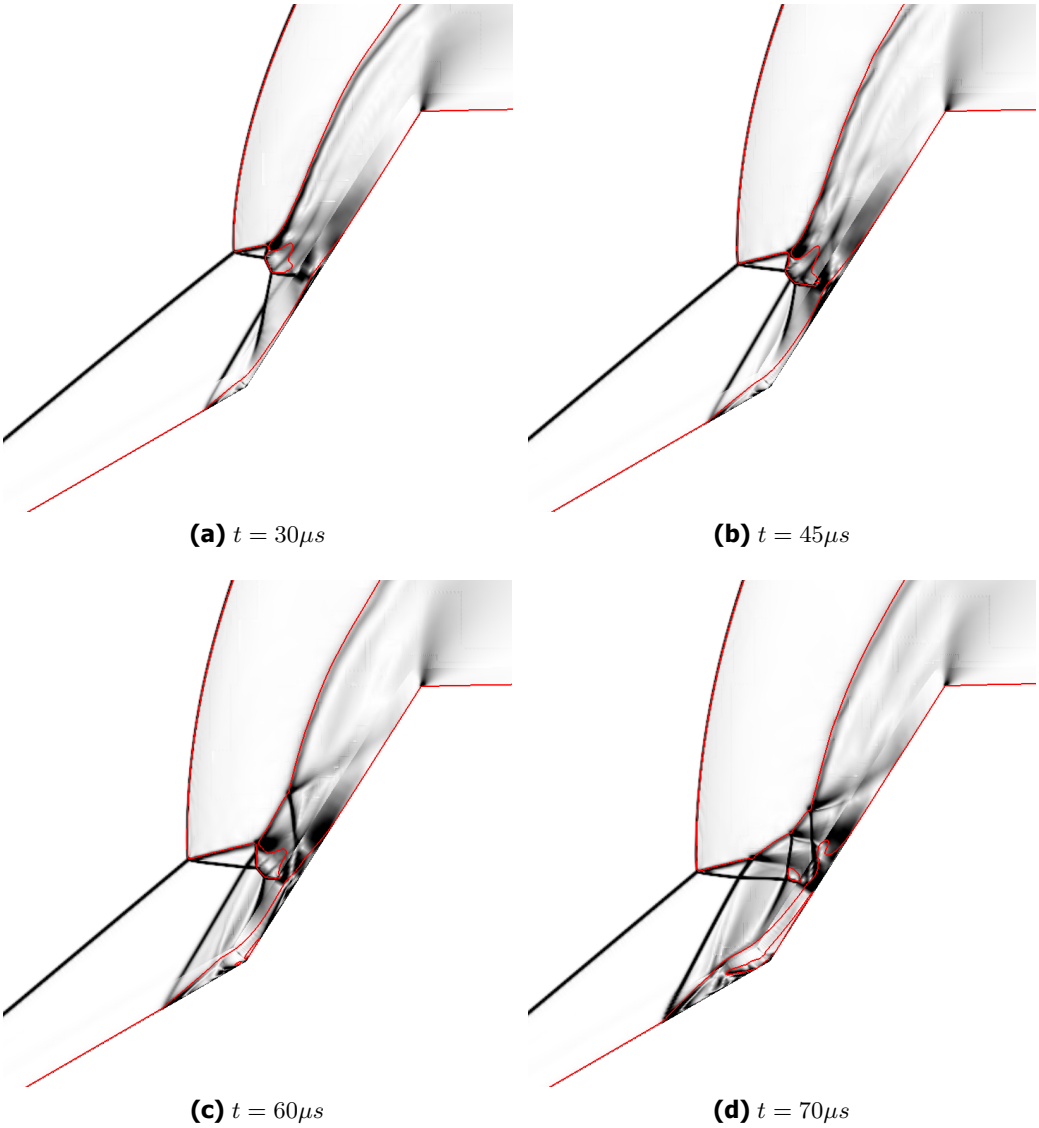

(a) $t = 30\mu s$ **(b)** $t = 45\mu s$

(c) $t = 60\mu s$ **(d)** $t = 70\mu s$

Fig 15. Density gradient computed with AMROC for the M7_8-N_2 case at several numerical times with $\theta_2 = 57.5°$

is a Type V-6S-2EW for the ideal gas.

One can also note that the curvature of the bow shock (BS) is more important as the thermochemical effects are reduced. This is because for a real gas the thermochemical effects (excitation of vibration modes, dissociation and recombination) absorb a significant part of the energy, so in the end the temperature is lower than that expected for an ideal gas. The oblique shock relation for temperature (1), which is only valid for constant γ, can be used to give an indication why the curvature is greater for reduced thermochemistry. For constant inflow conditions with Mach number M_1 and temperature T_1, lower temperature post-shock T_2 means a lower shock angle β, *i.e.* a lower curvature.

$$\frac{T_2}{T_1} = \frac{2\gamma(\gamma-1)M_1^2}{(\gamma+1)^2}\sin^2\beta \tag{1}$$

Moreover, recalling that the solid red lines on Fig. 16 are the sonic lines (*i.e.* Mach=1), one can note

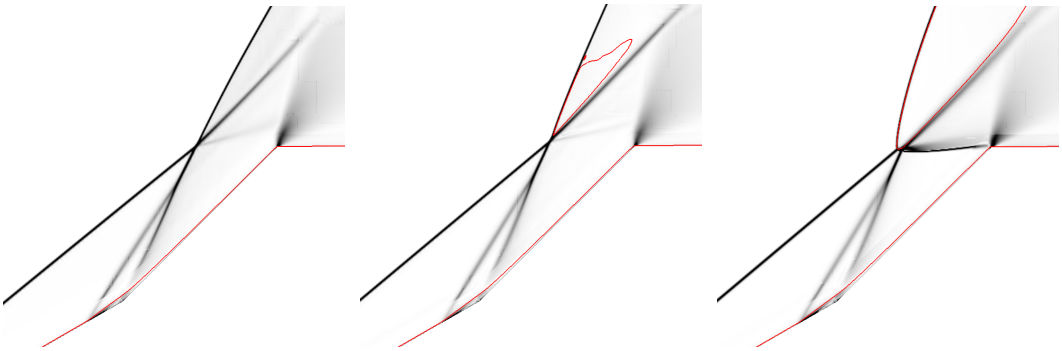

(a) Air **(b)** N_2 **(c)** Ideal Gas

Fig 16. Density gradient computed at $t = 120\mu s$ for air, N_2 and an Ideal Gas with inflow conditions M7_8 and a second wedge angle $\theta_2 = 45°$

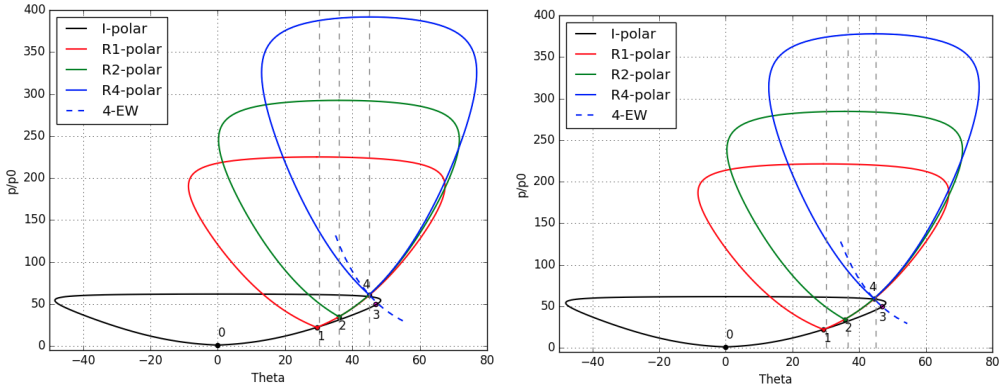

(a) Air **(b)** N_2

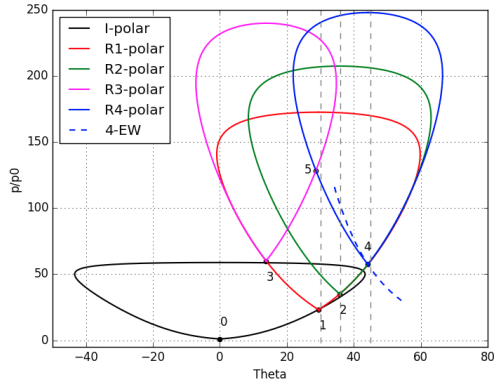

(c) Ideal Gas

Fig 17. Shock polar at $t = 120\mu s$ for air, N_2 and an Ideal Gas with inflow conditions M7_8 and a second wedge angle $\theta_2 = 45°$

that the flow is still supersonic behind the bow shock for air, whereas there is a subsonic area for N_2 and the ideal gas. This is likely because the curvature of the BS is more important as the thermochemical effects are reduced. A larger value of β means the oblique shock gets closer to a normal strong shock, behind which the flow is always subsonic.

The second example reported here is for $\theta_2 = 52.5°$, with density gradients for the three fluids shown

in Fig. 18 and associated shock polars in Fig. 19. As the second wedge angle has been increased from the previous example, the case for air is now a Type V-6S-2EW since the isentropic line 4-EW does not intersect the I-polar and the intersection or R3 and R4-polar is inside R1-polar. For N_2, the thermochemistry importance is reduced so the curvature of the BS is greater because for the reasons explained above. As a consequence, the Type V-6S-2EW shock pattern is more developed and the reattachment shock RS impinges the transmitted shock TS further down compared to air flow. For the ideal gas the shock pattern is a Type V, since there is a small Mach stem connecting the TS to the RS. This is because, as explained above, for lower thermochemistry effects the range of possible states behind a shock is reduced. Hence, the regular reflection of the TS and RS is not possible anymore and becomes a Mach reflection. This reflects on Fig. 19c by smaller shock polars compared to that on Fig. 19a and Fig. 19b, so R3 and R4 are not connected. Finally, no common possible state between the R3 and R4-polars exists, so there must be a Mach reflection.

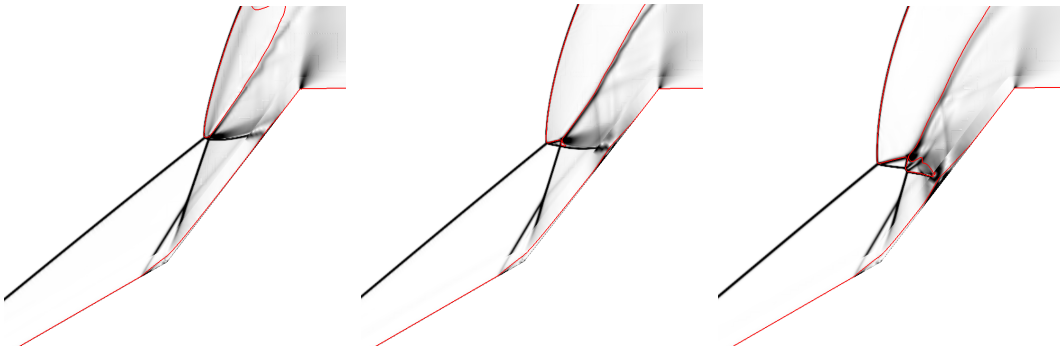

(a) Air **(b)** N_2 **(c)** Ideal Gas

Fig 18. Density gradient computed at $t = 40\mu s$ for air, N_2 and an Ideal Gas with inflow conditions M7_8 and a second wedge angle $\theta_2 = 52.5°$

To summarise, real gas modelling has a predominant effect on the shock pattern type computed. On the one hand, shock polars have shown that a lower degree of modelling of the thermochemistry ends up in a diminution of the range of the possible state behind shocks, in terms of total deflection angle θ and pressure ratio p/p_0. On the other hand, the more thermochemical effects are considered, the lower the post-shock temperature, involving a lower curvature of the bow shock. In the end, the θ_2 limit for Types VI $\leftrightarrow$ V-6S-2EW $\leftrightarrow$ V shock pattern transition is strongly dependent on the thermochemistry. This limit is the lowest for the highest degree of modelling (air flow), and *vice-versa*.

4. Criteria for Shock Pattern Transition

Shock patterns have been classified and the effect of thermochemistry modelling investigated. One could qualitatively show that there is an influence of three parameters on shock pattern transition. The first parameter of interest is the second wedge angle θ_2, which is responsible for a Type VI $\leftrightarrow$ V-6S-2EW $\leftrightarrow$ V transition, for sufficiently small times such as the SS still merges with the RS. Let us denote this instant as t_1. For $t > t_1$, the separation bubble in the boundary layer is sufficiently grown for the SS to directly impact the TS, leading to V-6S-2EW $\rightarrow$ V-6S-3EW and V $\rightarrow$ V-6S-3EW transitions. For even longer time, the SS will impinge the upper triple point (TP) formed by the leading edge shock (LS) and the bow shock (BS) at time t_2. This study is limited to shock pattern investigations for $t < t_2$, and to the best of our knowledge a Type VI remains unchanged until $t = t_2$. In addition to θ_2 and time, thermochemistry also plays a major role in the shock pattern transition, as it affects the limiting value of θ_2 for Type VI $\leftrightarrow$ V-6S-2EW $\leftrightarrow$ V transition. This section is to give quantitative information on the influence of these three parameters.

For a given fluid model, the pattern type is dependant on θ_2 and time, so one would like a criterion using those parameters as inputs, and returning the shock pattern as output. Numerous simulations have been done with different $\theta_2 \in [45°, 60°]$ for air, N_2 and an ideal gas. For every computed case,

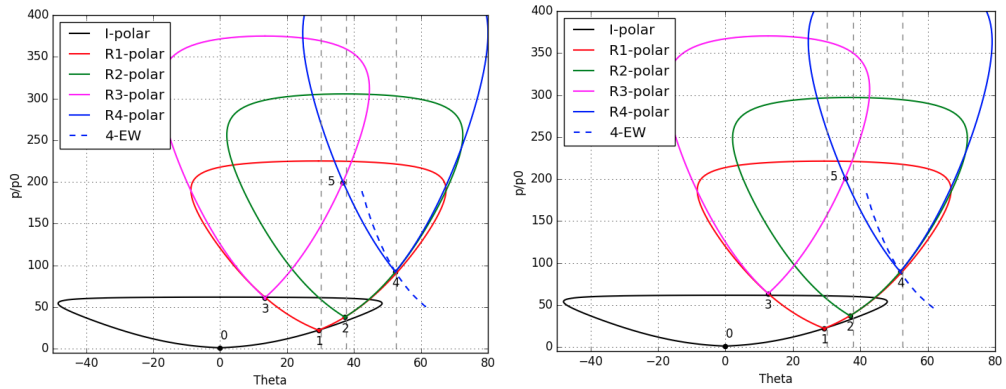

(a) Air **(b)** N_2

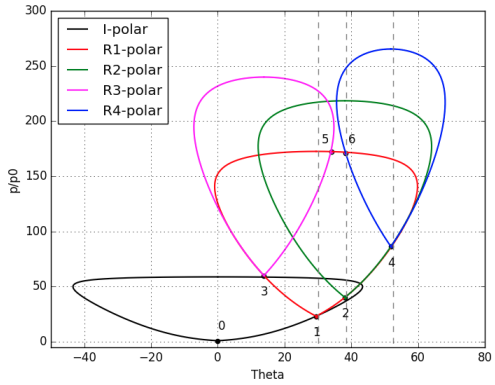

(c) Ideal Gas

Fig 19. Shock polar at $t = 40\mu s$ for air, N_2 and an Ideal Gas with inflow conditions M7_8 and a second wedge angle $\theta_2 = 52.5°$

the shock pattern has been manually checked every $5\mu s$ in the range of $t \in [30\mu s, 240\mu s]$, providing a shock pattern type mapping according to time and θ_2. This enabled us to draw the transition lines between each patterns on a (t, θ_2) diagram, see the solid black lines in Fig. 20. In this diagram is also reported the shock pattern mapping according to the shock polar theory, see the coloured areas. The main interest to compare the AMROC results to the shock polar code is that whereas AMROC gives an information on the actual shock pattern computed, the shock polar theory gives an information on the theoretically possible shock types. For example, the orange area on Fig. 20a indicates that both Type V-6S-2EW and Type V are possible in this range of time and θ_2, while the solid black lines determine the observed type. As already explained, AMROC simulations consider viscous flow whereas the shock polar analysis is limited to inviscid flow, therefore one needs to get the total deflection angle in region (2) from the simulations in order to build the shock polar. This region is the one behind the separation shock generated by the separation bubble. Moreover, the shock polar code requires to know if the SS still merges with the RS ($t < t_1$) or impinges the TS ($t_1 < t < t_2$). Hence, for a given $\theta_2 \in [45°, 60°]$, one gets the total deflection angle in region (2) as well as (t_1, t_2) from the AMROC simulations so as to conduct a shock polar analysis. Note that these values are directly related to the SS in the flow, and so to the development of the separation bubble upstream from the second wedge. In other words, building shock polars by getting the total deflection angle in region (2) and (t_1, t_2) from the AMROC results enables to apply inviscid shock polar analysis to viscous simulations.

For air, the Type VI to V-6S-2EW transition is poorly predicted by the shock polar theory, see Fig. 20a. The AMROC simulations indicate a limit of $\theta_2 = 49°$ whereas according to the shock polar theory the transition is around $\theta_2 = 46°$. The theory shows that both Type V-6S-2EW and Type V solutions are

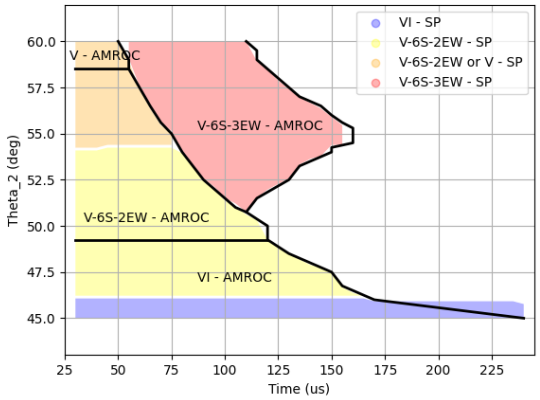

(a) Air

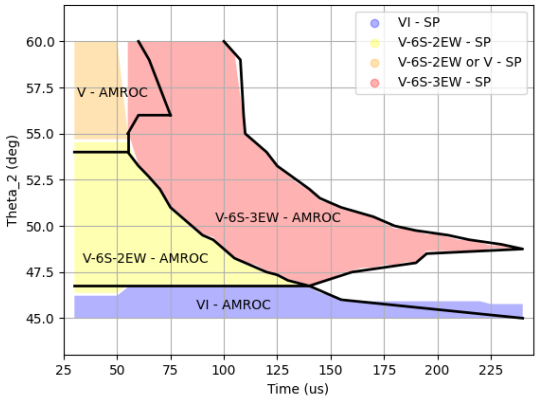

(b) N_2

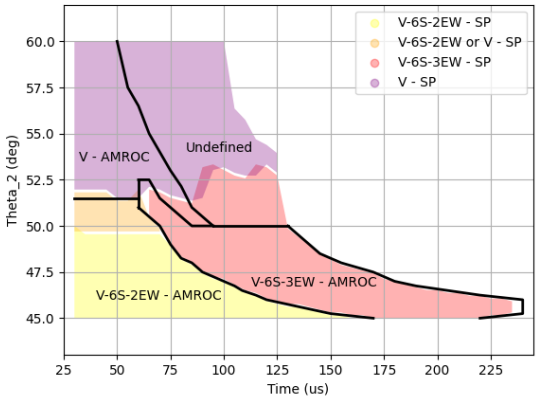

(c) Ideal Gas

Fig 20. Shock pattern types transition criteria with respect to time and second wedge angle θ_2 for air and N_2 with inflow conditions M7_8 according to the shock polar theory (coloured area) and AMROC simulations (black solid lines)

possible for $t < t_1$ in the range $\theta_2 = 54 - 60°$ (orange area). Indeed, they both exist in the simulations with a limit of $\theta_2 = 59°$ above which the pattern is a Type V, and below which it is still a Type V-6S-2EW. For $\theta_2 = 51° - 60°$ and $t_1 < t < t_2$ there is a Type V-6S-3EW pattern. Since (t_1, t_2) are extracted from the simulations and used to conduct the shock polar analysis, it is consistent to have good agreement between the AMROC results and the shock polar theory.

For the nitrogen flow, the Type VI to V-6S-2EW transition is well predicted around $\theta_2 = 46°$. For $\theta_2 > 54.5°$ and $t < t_1$, both Type V-6S-2EW and Type V are theoretically possible (orange area), even though the Type V solution prevails for $\theta_2 > 54°$ according to AMROC. For $\theta_2 = 56° - 60°$ the Type V subsists for a short time before becoming a Type V-6S-3EW pattern. Once the SS is above the Mach stem and impinges the TS at $t = t_1$, there is still a Mach reflection (MR) for approximately $15\mu s$ after which the MR vanishes and the shock pattern becomes a Type V-6S-3EW. The Fig. 15 shows the density gradient evolution for $\theta_2 = 57.5°$ and illustrates this phenomena. Although the simulations have shown a persistence of the Type V for a short duration for $t > t_1$, the shock polar theory never predicts the possibility for a Type V to occur for $t > t_1$. In other words, the observed Type V pattern is not supposed to exist anymore for $t > t_1$, which is likely why it disappears so quickly.

For the ideal gas, there is no Type VI for considered second wedge angle. There is a theoretical range in which both Types V-6S-2EW and V are possible (orange area), which is consistent with the observed Type V-6S-2EW for $\theta_2 < 52°$. Above this limit for $t < t_1$, the only theoretical solution is a Type V, and this limit matches with the computations. For $t > t_1$, once the MR disappears the shock patterns observed do not correspond to any type that would have been classified in this work. This is due to the too important development of the separation bubble, which is only obtained for the ideal gas with high θ_2 and long times. Since this case is only studied to show the importance of a real gas modelling but is not corresponding to real cases, no further investigations have been done to these specific patterns. Hence, this is referred as "undefined" in the Fig. 20c, even though the shock polar theory still predicts a Type V pattern (purple area).

To summarise, for the air and nitrogen flows, which are the cases of interest of this study since they can correspond to real application, the shock pattern is first driven by the second wedge angle for shorter times $t < t_1$. Figure 20 gives a pretty accurate information about the limiting θ_2 to have a transition between Types VI, V-6S-2EW and V. For longer times $t > t_1$, a shock pattern of Type V-6S-2EW or V becomes a Type V-6S-3EW. A potential Mach reflection can subsist for a short duration during this transition. An initial shock pattern of Type VI is steady until $t = t_2$. Note that this conclusion is only valid in the range of the study: $\theta_2 = 45 - 60°$ and $t_{max} = 240\mu s$, with the M7_8 inflow conditions and a first wedge angle $\theta_1 = 30°$. Also note that we have limited ourselves to $t < t_2$, *i.e.* the time at which the separation bubble is so developed that the separation bubble goes above the triple point.

5. Conclusion and Outlook

Simulations in the range of $\theta_2 = 45 - 60°$ for air, N_2 and an ideal gas were run in order to classify the shock patterns around a double wedge using our in-house code AMROC solving hypersonic viscous flow in thermochemical non-equilibrium. For sufficiently low second wedge angle, a Type VI occurs. This is a simple regular reflection of the leading edge shock (LS) with the reattachment shock (RS) generated by the reattachment of the separation bubble in the boundary layer just upstream of the compression corner of the double wedge. There is no transmitted shock (TS), just a weak expansion fan outgoing from the triple point (TP). For similar conditions, and as the second wedge angle is increased, a TS appears leading to a Type V-6S-2EW shock pattern. For longer time, the separation shock (SS) which initially merged with the RS impinges the TS, leading to a Type V-6S-3EW. Finally, for even greater θ_2, the regular reflection of the TS and the RS is not possible anymore and becomes a Mach reflection. This is the Type V pattern, which becomes a Type V-6S-3EW for longer time as the Mach stem vanishes once the SS has impinged the upper part of the TS.

This shock pattern classification has been supported by a shock polar analysis. The possibility to apply such an inviscid shock polar analysis to viscous simulations results has been demonstrated. Shock polars also enabled to better understand the influence of thermochemistry. For reduced thermochemical effects, the threshold θ_2 for Type VI $\leftrightarrow$ V-6S2EW and V-6S-2EW $\leftrightarrow$ V transition is lower.

Transition thresholds with respect to time have been drawn to summarise the influence of three parameters. The first influence is the one of θ_2, that drives the Type VI $\leftrightarrow$ V-6S2EW $\leftrightarrow$ V transition as the second wedge angle increases. There is good consistency between AMROC simulations and the shock polar code in terms of limiting θ_2. The second influence is that of viscosity, responsible for the boundary layer and its separation which generates a separation shock. Over time, this separation bubble grows, so the SS gets displaced upstream on the fore body. As a consequence, the impinging point of the SS on the RS is higher and higher, up to the point of impacting the TS. This leads to a Type V-6S-2EW $\rightarrow$ Type V-6S-3EW or Type V $\rightarrow$ V-6S-3EW transition for a constant θ_2 during time. The last parameter of influence studied is the thermochemistry. Thermochemical effects affects the limiting value of θ_2 for Type VI $\leftrightarrow$ V-6S-2EW $\leftrightarrow$ V transitions.

References

[1] B. Edney. Temperature measurements in a hypersonic gun tunnel using heat-transfer methods. Journal of fluid mechanics, 27(3):503–512, 1967.

[2] B. Edney. Anomalous heat transfer and pressure distributions on blunt bodies at hypersonic speeds in the presence of an impinging shock. Technical report, Flygtekniska Forsoksanstalten, Stockholm (Sweden), 1968.

[3] A. Swantek and J. Austin. Heat transfer on a double wedge geometry in hypervelocity air and nitrogen flows. In 50th AIAA Aerospace Sciences Meeting including the New Horizons Forum and Aerospace Exposition, page 284, 2012.

[4] J. Olejniczak, M.J. Wright, and G.V. Candler. Numerical study of inviscid shock interactions on double-wedge geometries. Journal of Fluid Mechanics, 352:1–25, 1997.

[5] J. Li, Y. Zhu, and X. Luo. On type VI-V transition in hypersonic double-wedge flows with thermo-chemical non-equilibrium effects. Physics of Fluids, 26(8):086104, 2014.

[6] A. Dufrene, M. Sharma, and J. Austin. Design and characterization of a hypervelocity expansion tube facility. Journal of Propulsion and Power, 23(6):1185–1193, 2007.

[7] A. Swantek and J. Austin. Flowfield establishment in hypervelocity shock-wave/boundary-layer interactions. AIAA Journal, 53(2):311–320, 2015.

[8] G. Pezzella, F. de Rosa, and R. Donelli. Computational analysis of shock wave boundary layer interactions in non-equilibrium hypersonic flow. In 20th AIAA International Space Planes and Hypersonic Systems and Technologies Conference, page 3578, 2015.

[9] A.S. Durna, M. El Hajj Ali Barada, and B. Celik. Shock interaction mechanisms on a double wedge at mach 7. Physics of Fluids, 28(9):096101, 2016.

[10] M.A. Badr and D.D. Knight. Shock wave laminar boundary layer interaction over a double wedge in a high mach number flow. In 52nd Aerospace Sciences Meeting, page 1136, 2014.

[11] J.R. Komives, I. Nompelis, and G.V. Candler. Numerical investigation of unsteady heat transfer on a double wedge geometry in hypervelocity flows. In 44th AIAA Fluid Dynamics Conference, page 2354, 2014.

[12] J. Hao, C.Y. Wen, and J. Wang. Numerical investigation of hypervelocity shock-wave/boundary-layer interactions over a double-wedge configuration. International Journal of Heat and Mass Transfer, 138:277–292, 2019.4

[13] J.D. Reinert, G.V. Candler, and J.R. Komives. Simulations of unsteady three-dimensional hypersonic double-wedge flow experiments. AIAA journal, 58(9):4055–4067, 2020.

[14] R. Deiterding. Block-structured adaptive mesh refinement-theory, implementation and application. In Esaim: Proceedings, volume 34, pages 97–150. EDP Sciences, 2011.

[15] C. Atkins and R. Deiterding. Towards a strand-Cartesian solver for modelling hypersonic flows in thermochemical non-equilibrium. In 23rd AIAA International Space Planes and Hypersonic Systems and Technologies Conference, 2020.

[16] J.B. Scoggins and T.E. Magin. Development of Mutation++: Multicomponent thermodynamic and transport properties for ionized plasmas written in C++. In 11th AIAA/ASME joint thermophysics and heat transfer conference, page 2966, 2014.

[17] R. Deiterding. High-resolution numerical simulation and analysis of mach reflection structures in detonation waves in low-pressure H2–O2–Ar mixtures: a summary of results obtained with the adaptive mesh refinement framework amroc. Journal of combustion, 2011.

[18] R.J. Kee, F.M. Rupley, and J.A. Miller. Chemkin-II: A fortran chemical kinetics package for the analysis of gas-phase chemical kinetics. Technical report, Sandia National Lab.(SNL-CA), Livermore, CA (United States), 1989.